A&A 549, A42 (2013)
DOI: 10.1051/0004-6361/201219835

Astronomy & Astrophysics

Atomic data for astrophysics: Fe XI soft X-ray lines⋆

G. Del Zanna[1] and P. J. Storey[2]

[1] DAMTP, Centre for Mathematical Sciences, Wilberforce Road, Cambridge, CB3 0WA, UK
e-mail: g.del-zanna@damtp.cam.ac.uk
[2] Department of Physics and Astronomy, University College London, Gower Street, London, WC1E 6BT, UK

Received 18 June 2012 / Accepted 16 November 2012

ABSTRACT

We present new large-scale R-matrix (up to $n = 4$) and distorted wave (up to $n = 6$) scattering calculations for electron collisional excitation of Fe XI. These data are needed for the analysis of soft X-ray spectra of astrophysical plasmas, where strong $n = 4 \rightarrow n = 3$ transitions are present. As found in previous work on Fe X, Fe XII, and Fe XIII, resonances from within the $n = 4$ levels and cascading from higher levels significantly increase the intensities of these lines. We provide a list of the strongest lines, many of which are unidentified. The present larger model produces intensities for decays from $n = 3$ levels mostly consistent with our previous work, however significant enhancements for some lower levels are found, in particular for the $3s^2\ 3p^3\ 3d\ ^5D$ which can be used to measure electron temperatures in the solar corona with the Hinode/EIS spectrometer.

Key words. atomic data – Sun: corona – line: identification – techniques: spectroscopic

1. Introduction

The soft X-ray (50–170 Å) spectrum of the quiet and active Sun is rich in $n = 4 \rightarrow n = 3$ transitions from highly ionised iron ions, from Fe VII to Fe XVI (see, e.g. Fawcett et al. 1968, 1972; Manson 1972; and Behring et al. 1976). Very little atomic data are currently available for these ions and the majority of the spectral lines still await firm identification, despite the fact that various instruments are routinely observing the soft X-rays, such as the Atmospheric Imaging Assembly (AIA, see Lemen et al. 2012), the Extreme ultraviolet Variability Experiment (EVE; Woods et al. 2012) on-board the Solar Dynamic Observatory (SDO) and the *Chandra* Low Energy Transmission Grating spectrometer (LETG, see Brinkman et al. 2000).

New atomic data for Fe VIII and Fe IX relevant for the soft X-rays have been presented in O'Dwyer et al. (2012). The importance of resonance effects for the $n = 4$ levels was found when calculating atomic data for Fe X (Del Zanna et al. 2012b), but was also found in Fe XII (Del Zanna et al. 2012a) and Fe XIII (Del Zanna & Storey 2012). Here, we present new large-scale scattering calculations for the Fe XI soft X-ray lines.

This paper is organised as follows. In Sect. 2, we give a brief review of previous observations and atomic calculations. In Sect. 3 we outline the methods we adopted for the scattering calculations. In Sect. 4 we present our results and in Sect. 5 we reach our conclusions.

2. Previous observations and atomic data for Fe XI

To our knowledge, the present results are the first R-matrix calculations for the Fe XI $n = 4$ levels. There are a number of atomic data calculations for the $n = 3$ levels, reviewed in the Iron Project work of Del Zanna et al. (2010, hereafter D10). That calculation included 145 LS terms and 465 fine-structure levels, and was aimed at providing accurate data for the main $n = 3$ levels. Three $J = 1$ levels in the $3s^2\ 3p^3\ 3d$ electron configuration proved particularly difficult to identify, despite producing strong lines in the EUV. A specific target was needed to calculate accurately the collision strengths for these levels.

Very limited atomic calculations for the Fe XI $n = 4$ levels have been available up to now, with just a few configurations considered. For example, Bhatia et al. (2002) presented a scattering calculation which included the $3s^2\ 3p^3\ 4s$ and $3s^2\ 3p^3\ 4d$ levels using the distorted wave (DW) code developed at University College London.

The D10 atomic data were benchmarked against well-calibrated observations in Del Zanna (2010). The main long-standing discrepancies were finally resolved, and a large number of new energy levels were identified. These new $n = 3$ energies, adopted here, were obtained from a careful assessment of all available wavelength measurements.

The identifications of some of the $3s^23p^2\ 4s$ levels are due to the seminal laboratory work by Edlén (1937). The identifications of some of the $3s^23p^2\ 4l$ (l = p, d, f) levels are due to the fundamental work by Fawcett et al. (1972), using laboratory spectra in the soft X-rays of $n = 4 \rightarrow n = 3$ transitions. A few transitions were only tentatively identified, and the spectra contain a large number of unidentified lines.

We have re-analysed some of Fawcett's plates as part of a larger project to complete the identification work on the Fe soft X-ray spectrum. The atomic data presented here have been benchmarked against Fawcett's plates and solar observations. Several of the strongest lines have been identified. Details are provided in Del Zanna (2012). Some of these new identifications have been included in a recent release of the CHIANTI atomic database (Landi et al. 2012).

⋆ The full dataset is only available at the CDS via anonymous ftp to cdsarc.u-strasbg.fr (130.79.128.5) or via http://cdsarc.u-strasbg.fr/viz-bin/qcat?J/A+A/549/A42

3. Methods

The atomic structure calculations were carried out using the AUTOSTRUCTURE program (Badnell 1997) which constructs target wavefunctions using radial wavefunctions calculated in a scaled Thomas-Fermi-Dirac statistical model potential with a set of scaling parameters.

The Breit-Pauli distorted wave calculations were carried out using the recent development of the AUTOSTRUCTURE code, described in detail in Badnell (2011). Collision strengths are calculated at the same set of final scattered energies for all transitions. "Top-up" for the contribution of high partial waves is done using the same Breit-Pauli methods and subroutines implemented in the R-matrix outer-region code STGF. The program also provides radiative rates and infinite energy Born limits. These limits are particularly important for two reasons. First, they allow a consistency check on the collision strengths in the scaled Burgess & Tully (1992) domain (see also Burgess et al. 1997). Second, they are used in the interpolation of the collision strengths at high energies when calculating the Maxwellian averages.

The R-matrix method used in the inner region of the scattering calculation is described in Hummer et al. (1993) and Berrington et al. (1995). We performed the calculation in *LS* coupling and included the mass-velocity and Darwin relativistic operators. The outer region calculation used the intermediate-coupling frame transformation (ICFT) method by Griffin et al. (1998). Dipole-allowed transitions were topped-up to infinite partial wave using an intermediate coupling version of the Coulomb-Bethe method as described by Burgess (1974) while non-dipole allowed transitions were topped-up assuming that the collision strengths form a geometric progression in J (see Badnell & Griffin 2001). The collision strengths were extended to high energies by interpolation using the appropriate high-energy limits in the Burgess & Tully (1992) scaled domain. The high-energy limits were calculated with AUTOSTRUCTURE for both optically-allowed (see Burgess et al. 1997) and non-dipole allowed transitions (see Chidichimo et al. 2003). The temperature-dependent effective collisions strength $\Upsilon(i - j)$ were calculated by assuming a Maxwellian electron energy distribution.

4. Results

4.1. The R-matrix and DW calculations for the n = 3, 4 levels

We performed preliminary DW calculations systematically increasing the number of configurations up to and including those with $n = 6$ valence orbitals. We also carried out separate structure calculations for each case to calculate all of the radiative data for all transitions among the levels. This ensures that all the cascading from the target configurations is included. We then calculated the level populations in equilibrium and the relative line intensities so as to find out which lines are expected to be strongest, to identify the spectroscopically important configurations. We then followed the procedure outlined in the Fe X case to estimate which configurations would be likely to be producing resonances in the collision strengths for the spectroscopically important configurations and levels.

As our configuration basis set we have chosen the set of $n = 3, 4$ configurations shown in Fig. 1 and listed in Table 1. The scaling parameters λ_{nl} for the potentials in which the orbital functions are calculated are also given in Table 1. These potential scaling parameters were obtained in four stages. In the first three stages, the sum of all the energies in the 36 configurations was minimised and the scaling parameters were varied in groups according to n. In the fourth and final stage the scaling parameters for the 3s, 3p and 3d orbitals alone were varied to make the sum of the energies of the energetically lowest 20 terms a minimum. A full R-matrix calculation with all the $n = 4$ levels is currently prohibitive, because it would involve 5262 fine-structure levels. For the scattering close-coupling calculation, we retained the main configurations and levels, including all the $3s^2\ 3p^3\ 4l$ (l = s, p, d, f) levels and almost all of the $3s\ 3p^3\ 3d\ 4l$ (l = s, p, d, f) ones, giving 996 fine-structure levels within 18 configurations arising from the energetically lowest 408 *LS* terms (see Fig. 1). This is a significant expansion compared to the previous calculation we performed (145 *LS* terms). We have performed both an ICFT R-matrix (RM4) and a DW calculation (DW4) using the same basis.

Table 1. Target electron configuration basis and orbital scaling parameters λ_{nl} for the R-matrix and DW runs.

Configurations	λ_{nl}	
$3s^2\ 3p^4$	1s	1.41599
$3s^2\ 3p^3\ 3d$	2s	1.12134
$3s^2\ 3p^3\ 4l$ (l = s, p, d, f)	2p	1.06602
$3s^2\ 3p^2\ 3d^2$	3s	1.12436
$3s^2\ 3p^2\ 3d\ 4l$ (l = s, p, d, f)	3p	1.09803
$3s^2\ 3p\ 3d^3$	3d	1.11459
$3s\ 3p^5$	4s	1.17694
$3s\ 3p^4\ 3d$	4p	1.14795
$3s\ 3p^4\ 4l$ (l = s, p, d, f)	4d	1.16345
$3s\ 3p^3\ 3d\ 4l$ (l = s, p, d, f)	4f	1.42572
$3s\ 3p^2\ 3d^3$	5s	1.17376
$3p^5\ 3d$	5p	1.05304
$3p^5\ 4l$ (l = s, p, d, f)	5d	1.14911
$3p^4\ 3d^2$	5f	1.28690
$3p^4\ 3d\ 4l$ (l = s, p, d, f)	5g	1.57031
$3p^3\ 3d^3$	6s	1.15709
$3s^2\ 3p^3\ 5l$ (l = s, p, d, f, g)	6p	1.19019
$3s\ 3p^4\ 5l$ (l = s, p, d, f,g)	6d	1.26478
$3p^5\ 5l$ (l = s, p, d, f, g)	6f	1.27665
$3s^2\ 3p^3\ 6l$ (l = s, p, d, f, g)	6g	1.22464
$3s\ 3p^4\ 6l$ (l = s, p, d, f, g)		
$3p^5\ 6l$ (l = s, p, d, f, g)		

Notes. The configurations above the line were used for the RM4 and DW4 calculations. Those below the line were added for the DW calculation DW6.

Tables 2, 3 present a selection of fine-structure target level energies E_t, compared to experimental energies E_{exp}. The latter have been obtained from Del Zanna (2010) for the $n = 3$ levels, otherwise from the measurements of Edlén (1937) and Fawcett et al. (1972). Some of the experimental energies of Fawcett et al. (1972) have been slightly revised in the benchmark study of Del Zanna (2012), where also additional lines and levels have been identified.

There is good overall agreement in terms of energy differences between levels when considering both the observed and the target energies, for the present and the previous calculation. However, the present target fails to provide accurate values for the three $J = 1$ levels in the $3s^2\ 3p^3\ 3d$ electron configuration (levels 37, 39, 41).

A set of "best" energies E_b was obtained with a linear fit between the E_{exp} and E_t values. The E_b values were used (together with the E_{exp} ones) within the R-matrix calculation to obtain an

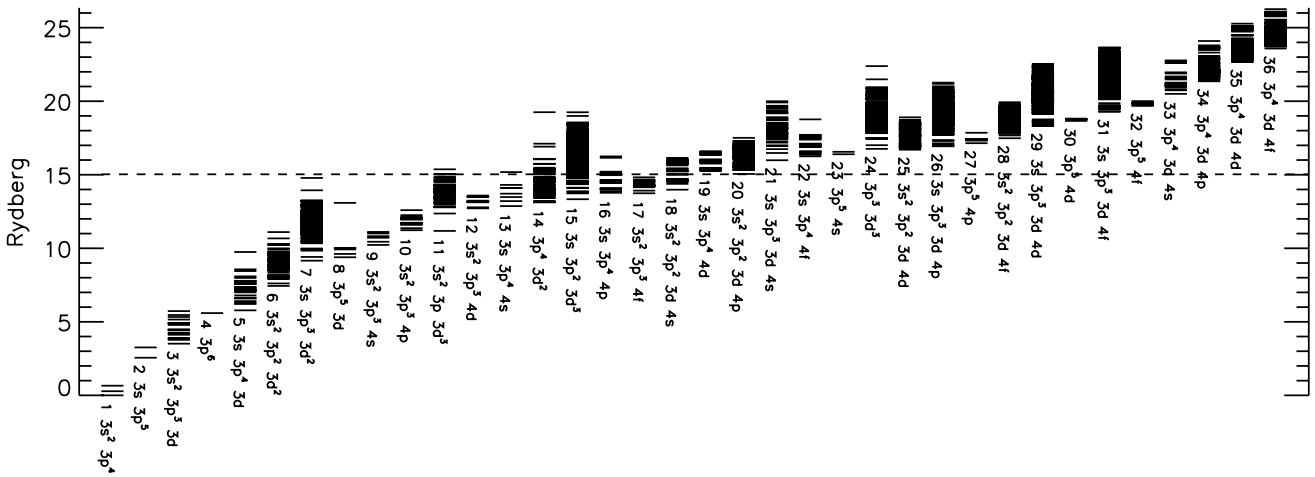

Fig. 1. Term energies of the target levels (36 configurations) for the $n = 4$ calculations. The 408 terms within the lowest 18 configurations which produce levels having energies below the dashed line have been retained for the close-coupling expansion.

accurate position of the resonance thresholds. They were also used to calculate the transition probabilities, which was done separately.

The expansion of each scattered electron partial wave was done over a basis of 20 functions within the R-matrix boundary and the partial wave expansion extended to a maximum total orbital angular momentum quantum number of $L = 16$. This produces reliable collision strengths up to about 80 Ryd.

The outer region calculation includes exchange up to a total angular momentum quantum number $J = 26/2$. We have supplemented the exchange contributions with a non-exchange calculation extending from $J = 27/2$ to $J = 73/2$. The outer region exchange calculation was performed in a number of stages. A coarse energy mesh was chosen above all resonances. The resonance region itself was calculated with 8000 points.

4.2. The n = 3 levels and the EUV lines

We then compared the thermally-averaged collision strengths with our previous R-matrix results for the $n = 3$ levels. Note that the ordering of the levels 27, 28 and 47, 48 in the present calculation is inverted, compared to D10. Good agreement is found at coronal temperatures. As an example, Fig. 2 shows a comparison between the present thermally-averaged collision strengths at 1.26 MK, compared to those of D10, for all transitions between the ground configuration levels and those up to level 47 (i.e. all among $3s^2\ 3p^4$ and between $3s^2\ 3p^4$ and $3s\ 3p^5$, $3s^2\ 3p^3\ 3d$). Only transitions to levels 37, 39, 41 (the three $3s^2\ 3p^3\ 3d\ J = 1$ problematic levels) were omitted. At lower temperatures (e.g. 0.5 MK), the present collision strengths for the weaker transitions are progressively higher, indicating some resonance enhancement due to the larger target.

We also compared the line intensities obtained from the present (RM4) and our previous D10 model for the $n = 3$ transitions, finding very small increases (less than 10%) for most among the stronger transitions. A few transitions were however found to be significantly enhanced. They are listed in Table 4. The decays from the $3s^2\ 3p^3\ 3d\ ^5D$ levels (around 257 Å) are of particular importance for Hinode/EIS. They were identified in D10, where it was also shown that they can in principle be used to measure electron temperatures in the solar corona around 1 MK. One problem found in D10 was that the temperatures were considerably lower than expected, due to too low predicted emissivities. The increased intensities produced with the present model are a significant improvement. Some differences between the previous and the present models in terms of line intensities are due to different A-values. The lines displayed in Table 4 have very small A-values, and some are sensitive to the target structure being considered, such as the 1–16. However, the main changes in the line intensities are due to enhanced populations.

A natural question then arises: what causes these enhanced populations only for these levels? The levels most affected are among the lowest of the $3s^2\ 3p^3\ 3d$ configuration, hence likely candidates are enhanced resonances provided by the much larger scattering target, and increased cascading again due to the larger number of levels. To look for the main effects, we have looked at how each of the upper levels in Table 4 is mainly populated, and how the population and cascading changes from the previous to the present model.

The changes are subtle, as we also found for Fe XII. Overall, there is a clear increase in the populations due to increased cascading in the present model. Indeed, for many levels, cascading is an important or even dominant populating mechanism. The increased populations are caused by the cumulative effect of small increases in the populations of higher levels (due to slightly increased excitations due to extra resonances), and by the larger number of levels included in the present model. We have also found that the main cascading effects are due to $n = 4$ levels, indeed adding cascading from the main $n = 5, 6$ levels changes the populations only slightly (less than 10%), as is also clear from comparing the line intensities calculated with the RM4 and RM4 + DW6 models in Table 4. This gives us confidence in the reliability of our RM4 + DW6 model for this ion. Any further cascading from higher levels is expected to produce even smaller increases.

As an example, we briefly discuss level 14 ($3s^2\ 3p^3\ 3d\ ^5D_4$). This is a metastable level having a small (36 s^{-1}) transition probability to the ground state. Its intensity is increased by 20% with the present RM4 model (see Table 4). As shown in Table 5, only 27% of its population comes from direct excitation from the ground state (with the RM4 model). As shown in Fig. 3, the collision strength for this latter transition is the same as previously calculated, so the increased population is due solely to cascading. The main cascading comes from levels 21 and 23, as shown in Table 5. In turn, the main cascading for level 21 is

Table 2. Level energies for Fe XI ($n = 3$).

i	Conf.	Lev.	E_{exp}	E_t	E_t (D10)
1	$3s^2\ 3p^4$	$^3P_2$	0.000	0.000	0.000
2	$3s^2\ 3p^4$	$^3P_1$	0.115	0.112 (0.004)	0.115 (0.001)
3	$3s^2\ 3p^4$	$^3P_0$	0.130	0.129 (0.002)	0.130 (0.001)
4	$3s^2\ 3p^4$	$^1D_2$	0.344	0.357 (−0.013)	0.360 (−0.016)
5	$3s^2\ 3p^4$	$^1S_0$	0.737	0.753 (−0.016)	0.731 (0.006)
6	$3s\ 3p^5$	$^3P_2$	2.584	2.574 (0.010)	2.547 (0.037)
7	$3s\ 3p^5$	$^3P_1$	2.671	2.660 (0.011)	2.635 (0.036)
8	$3s\ 3p^5$	$^3P_0$	2.726	2.713 (0.013)	2.689 (0.037)
9	$3s\ 3p^5$	$^1P_1$	3.297	3.327 (−0.029)	3.304 (−0.006)
10	$3s^2\ 3p^3\ 3d$	$^5D_0$	3.532	3.554 (−0.023)	3.518 (0.014)
11	$3s^2\ 3p^3\ 3d$	$^5D_1$	3.533	3.557 (−0.023)	3.520 (0.013)
12	$3s^2\ 3p^3\ 3d$	$^5D_2$	3.535	3.559 (−0.024)	3.523 (0.012)
13	$3s^2\ 3p^3\ 3d$	$^5D_3$	3.538	3.564 (−0.025)	3.527 (0.011)
14	$3s^2\ 3p^3\ 3d$	$^5D_4$	3.547	3.573 (−0.026)	3.537 (0.010)
15	$3s^2\ 3p^3\ 3d$	$^3D_2$	3.762	3.806 (−0.044)	3.767 (−0.004)
16	$3s^2\ 3p^3\ 3d$	$^3D_3$	3.786	3.827 (−0.041)	3.790 (−0.005)
17	$3s^2\ 3p^3\ 3d$	$^3D_1$	3.800	3.841 (−0.040)	3.805 (−0.004)
18	$3s^2\ 3p^3\ 3d$	$^3F_2$	3.853	3.900 (−0.047)	3.863 (−0.009)
19	$3s^2\ 3p^3\ 3d$	$^1S_0$	–	3.919	3.885
20	$3s^2\ 3p^3\ 3d$	$^3F_3$	3.882	3.931 (−0.049)	3.895 (−0.013)
21	$3s^2\ 3p^3\ 3d$	$^3F_4$	3.923	3.974 (−0.050)	3.939 (−0.016)
22	$3s^2\ 3p^3\ 3d$	$^3G_3$	–	4.157	4.122
23	$3s^2\ 3p^3\ 3d$	$^3G_4$	4.103	4.173 (−0.070)	4.138 (−0.036)
24	$3s^2\ 3p^3\ 3d$	$^3G_5$	4.123	4.194 (−0.071)	4.161 (−0.039)
25	$3s^2\ 3p^3\ 3d$	$^1G_4$	4.185	4.263 (−0.078)	4.226 (−0.042)
26	$3s^2\ 3p^3\ 3d$	$^1D_2$	–	4.316	4.269
27	$3s^2\ 3p^3\ 3d$	$^3P_0$	–	4.459	4.412
28	$3s^2\ 3p^3\ 3d$	$^3D_1$	–	4.460	4.412
29	$3s^2\ 3p^3\ 3d$	$^3P_1$	4.418	4.484 (−0.066)	4.437 (−0.019)
30	$3s^2\ 3p^3\ 3d$	$^3F_3$	4.420	4.493 (−0.073)	4.451 (−0.031)
31	$3s^2\ 3p^3\ 3d$	$^3F_2$	–	4.502	4.459
32	$3s^2\ 3p^3\ 3d$	$^3F_4$	4.433	4.505 (−0.073)	4.466 (−0.033)
33	$3s^2\ 3p^3\ 3d$	$^3D_2$	4.460	4.531 (−0.071)	4.487 (−0.027)
34	$3s^2\ 3p^3\ 3d$	$^3P_2$	4.502	4.568 (−0.066)	4.525 (−0.023)
35	$3s^2\ 3p^3\ 3d$	$^3D_3$	4.531	4.604 (−0.072)	4.561 (−0.030)
36	$3s^2\ 3p^3\ 3d$	$^1F_3$	4.787	4.874 (−0.087)	4.833 (−0.046)
37	$3s^2\ 3p^3\ 3d$	$^1P_1$	4.839	4.933 (−0.094)	4.892 (−0.052)
38	$3s^2\ 3p^3\ 3d$	$^3P_2$	4.842	4.934 (−0.092)	4.894 (−0.052)
39	$3s^2\ 3p^3\ 3d$	$^3S_1$	4.861	4.971 (−0.110)	4.923 (−0.061)
40	$3s^2\ 3p^3\ 3d$	$^3P_0$	4.937	5.027 (−0.090)	4.990 (−0.053)
41	$3s^2\ 3p^3\ 3d$	$^3P_1$	4.934	5.028 (−0.094)	4.991 (−0.057)
42	$3s^2\ 3p^3\ 3d$	$^3D_3$	5.051	5.167 (−0.116)	5.119 (−0.067)
43	$3s^2\ 3p^3\ 3d$	$^3D_2$	5.118	5.234 (−0.116)	5.188 (−0.070)
44	$3s^2\ 3p^3\ 3d$	$^3D_1$	5.161	5.275 (−0.114)	5.231 (−0.069)
45	$3s^2\ 3p^3\ 3d$	$^1D_2$	5.275	5.407 (−0.131)	5.356 (−0.081)
46	$3s^2\ 3p^3\ 3d$	$^1F_3$	5.413	5.541 (−0.128)	5.502 (−0.088)
47	$3p^6$	$^1S_0$	–	5.655	5.751
48	$3s^2\ 3p^3\ 3d$	$^1P_1$	5.678	5.811 (−0.133)	5.818 (−0.140)
54	$3s\ 3p^4\ 3d$	$^5F_5$	6.339	6.231 (0.108)	6.345 (−0.005)
67	$3s\ 3p^4\ 3d$	$^3F_4$	6.735	6.644 (0.090)	6.755 (−0.020)
68	$3s\ 3p^4\ 3d$	$^3D_3$	–	6.666	6.771
72	$3s\ 3p^4\ 3d$	$^3G_4$	–	6.858	7.000
74	$3s\ 3p^4\ 3d$	$^1G_4$	–	7.067	7.166
79	$3s\ 3p^4\ 3d$	$^3D_3$	7.339	7.230 (0.109)	7.355 (−0.016)
91	$3s\ 3p^4\ 3d$	$^3F_4$	–	7.618	7.739
147	$3s^2\ 3p^2\ 3d^2$	$^3F_4$	–	8.705	8.863
161	$3s^2\ 3p^2\ 3d^2$	$^3H_6$	–	8.903	9.066
178	$3s^2\ 3p^2\ 3d^2$	$^1G_4$	–	9.228	9.366

Notes. The experimental level energies E_{exp} (in Rydbergs, from Del Zanna 2010) are shown, together with those obtained from our scattering target E_t and those from the previous scattering calculation (D10). Values in parentheses indicate differences with E_{exp}. Only a selection of levels is shown.

Table 3. Level energies for Fe XI ($n = 4$).

i	Conf.	Lev.	E_{exp}	E_t
265	$3s^2\ 3p^3\ 4s$	$^3S_1$	10.218	10.493 (−0.275)
288	$3s^2\ 3p^3\ 4s$	$^3D_1$	10.467	10.754 (−0.287)
289	$3s^2\ 3p^3\ 4s$	$^3D_2$	10.471	10.758 (−0.286)
291	$3s^2\ 3p^3\ 4s$	$^3D_3$	10.502	10.782 (−0.280)
295	$3s^2\ 3p^3\ 4s$	$^1D_2$	10.578	10.871 (−0.293)
334	$3s^2\ 3p^3\ 4s$	$^1P_1$	10.888	11.203 (−0.315)
345	$3s^2\ 3p^3\ 4p$	$^5P_2$	11.023	11.263 (−0.240)
353	$3s^2\ 3p^3\ 4p$	$^5P_3$	11.052	11.296 (−0.244)
377	$3s^2\ 3p^3\ 4p$	$^3P_2$	–	11.426
423	$3s^2\ 3p^3\ 4p$	$^1F_3$	11.491	11.784 (−0.293)
424	$3s^2\ 3p^3\ 4p$	$^3F_4$	11.502	11.786 (−0.284)
454	$3s^2\ 3p^3\ 4p$	$^3P_2$	11.644*	12.031(−0.386)
460	$3s^2\ 3p^3\ 4p$	$^3D_2$	11.794	12.074 (−0.279)
527	$3s^2\ 3p^3\ 4d$	$^5D_4$	–	12.770
536	$3s^2\ 3p^3\ 4d$	$^3D_3$	12.546	12.838 (−0.292)
596	$3s\ 3p^4\ 4s$	$^3P_2$	12.831*	13.231(−0.400)
606	$3s^2\ 3p^3\ 4d$	$^1D_2$	12.946	13.267 (−0.321)
616	$3s^2\ 3p^3\ 4d$	$^1F_3$	12.971	13.300 (−0.329)
702	$3s^2\ 3p^3\ 4f$	$^5F_4$	13.483	13.791 (−0.308)
704	$3s^2\ 3p^3\ 4f$	$^5F_5$	13.481	13.792 (−0.311)
749	$3s^2\ 3p^3\ 4f$	$^3F_4$	–	13.979
800	$3s^2\ 3p^3\ 4f$	$^3G_4$	13.844	14.198 (−0.354)
801	$3s\ 3p^2\ 3d^3$	$^5H_7$	–	14.216
802	$3s^2\ 3p^3\ 4f$	$^3G_5$	13.868	14.227 (−0.358)
810	$3s^2\ 3p^3\ 4f$	$^3H_6$	13.935	14.292 (−0.357)
813	$3s^2\ 3p^3\ 4f$	$^3F_4$	–	14.313
891	$3s^2\ 3p^3\ 4f$	$^3G_4$	14.232	14.618 (−0.386)
898	$3s^2\ 3p^3\ 4f$	$^3G_5$	14.251	14.626 (−0.375)

Notes. Same as Table 2. The experimental level energies E_{exp} are from Fawcett et al. (1972). Values indicated with * are from Del Zanna (2012). Also note that additional levels have been tentatively identified by Del Zanna (2012), and some energies revised.

from level 24. Levels 21, 23, 24 are populated by 27%, 54%, and 53% from the ground state, respectively. Figure 3 shows that the collision strengths for these transitions from the ground state are enhanced in the present model, which explains part of the increased population for level 14. The rest is due to cascading to levels 21, 23, and 24 from a host of levels (the main ones being 32, 67, 68, 72, 79, 91, 147, 161, 424), all within the $n = 4$ model. These levels are mostly populated from the ground state, and have increased collision strengths in the present calculation, due to the larger target. The population and cascading effects are only slightly increased when the $n = 5, 6$ configurations are included (model RM4 + DW6).

The other important $3s^2\ 3p^3\ 3d\ ^5D$ levels are not strictly metastable, and about half of their population is due to direct excitation from the ground state. As for level 14, the collision strengths for these excitations are virtually the same as previously calculated, so the increased populations is mainly caused by cascading, again mostly due to $n = 4$ levels which have increased collision strengths due to resonance enhancements.

4.3. The n = 4 levels and the soft X-ray lines

We have constructed an ion population model (RM4) with the new R-matrix rates, complemented with a set of A-values calculated separately with exactly the same target, but with the experimental and best energies. We did the same with the DW collision strengths, building an ion model (DW4) with the same set of A-values. Table 6 shows the collision strengths for a sample of

Table 4. Relative intensities of a few key Fe XI EUV lines.

$i-j$	Levels	I(D10)	I(RM4)	I(RM4+DW6)	gf	A_{ji}(D10)	A_{ji}	λ_{exp}
1–42	$3s^2\ 3p^4\ {}^3P_2$–$3s^2\ 3p^3\ 3d\ {}^3D_3$	1.0	1.0	1.0	4.82	1.4×10^{11}	1.4×10^{11}	180.401
1–14	$3s^2\ 3p^4\ {}^3P_2$–$3s^2\ 3p^3\ 3d\ {}^5D_4$	0.083	0.10	0.11	–	35.	36.	256.919
1–16	$3s^2\ 3p^4\ {}^3P_2$–$3s^2\ 3p^3\ 3d\ {}^3D_3$	5.8×10^{-2}	7.2×10^{-2}	7.7×10^{-2}	1.1×10^{-4}	2.6×10^{6}	1.8×10^{6}	240.717
1–13	$3s^2\ 3p^4\ {}^3P_2$–$3s^2\ 3p^3\ 3d\ {}^5D_3$	4.1×10^{-2}	5.6×10^{-2}	6.0×10^{-2}	1.4×10^{-3}	2.1×10^{7}	2.0×10^{7}	257.554
4–21	$3s^2\ 3p^4\ {}^1D_2$–$3s^2\ 3p^3\ 3d\ {}^3F_4$	2.6×10^{-2}	3.9×10^{-2}	4.0×10^{-2}	–	57.	57.	254.596
1–12	$3s^2\ 3p^4\ {}^3P_2$–$3s^2\ 3p^3\ 3d\ {}^5D_2$	2.5×10^{-2}	3.0×10^{-2}	3.2×10^{-2}	2.9×10^{-3}	6.4×10^{7}	5.7×10^{7}	257.772
4–16	$3s^2\ 3p^4\ {}^1D_2$–$3s^2\ 3p^3\ 3d\ {}^3D_3$	1.9×10^{-2}	2.8×10^{-2}	2.9×10^{-2}	5.2×10^{-5}	8.3×10^{5}	6.9×10^{5}	264.772
1–35	$3s^2\ 3p^4\ {}^3P_2$–$3s^2\ 3p^3\ 3d\ {}^3D_3$	1.6×10^{-2}	2.6×10^{-2}	2.7×10^{-2}	1.9×10^{-2}	5×10^{8}	4.5×10^{8}	201.112
4–20	$3s^2\ 3p^4\ {}^1D_2$–$3s^2\ 3p^3\ 3d\ {}^3F_3$	1.5×10^{-2}	2.1×10^{-2}	2.2×10^{-2}	7.1×10^{-4}	1.1×10^{7}	1.0×10^{7}	257.547

Notes. The lines are displayed in decreasing order of intensity (photons) $I = N_j A_{ji}/N_e$ relative to the strongest EUV line. The intensities were calculated at log T_e [K] = 6.15 and log N_e [cm^{-3}] = 8. with the previous (D10) and the present (RM4) model. The remaining columns show the gf and A(s^{-1}) values calculated in the previous and present work, and the experimental wavelengths λ_{exp}(Å) following the identifications in D10.

Table 5. Populations of a few key levels arising from the $3s^2\ 3p^3\ 3d$ configuration.

i	Lev.	POP(%) D10	RD(%) D10	EXC(%) D10	POP(%) RM4	RD(%) RM4	EXC(%) RM4	POP(%) RM4 + DW6	RD(%) RM4 + DW6	EXC(%) RM4 + DW6
14	$3s^2\ 3p^3\ 3d\ {}^5D_4$	0.13	63	37	0.167	72	28	0.176	73	27
			15.3(21)	36(1)		15.5(21)	27(1)		15.3(21)	25(1)
			12.0(23)			12.4(23)			12.2(23)	
			8.7(25)			9.4(25)			9.4(25)	
21	$3s^2\ 3p^3\ 3d\ {}^3F_4$	2.6×10^{-2}	65	35	4.0×10^{-2}	71	28	4.1×10^{-2}	73	27
			30.4(24)	33(1)		31.5(24)	27(1)		31.5(24)	26(1)
			9.6(79)			7.1(23)			7.1(23)	
			6.8(23)			6.8(79)			6.7(79)	
			5.3(68)			3.4(68)			3.5(68)	
23	$3s^2\ 3p^3\ 3d\ {}^3G_4$	5.0×10^{-2}	30	69	8.4×10^{-2}	42	58	8.8×10^{-2}	44	55
			4.7(67)	65(1)		4.8(32)	54(1)		4.8(32)	51(1)
			4.6(32)			3.4(67)			3.7(72)	
			2.5(24)			3.4(72)			3.5(67)	
24	$3s^2\ 3p^3\ 3d\ {}^3G_5$	0.15	28	72	0.24	45	55	0.25	47	53
			6.4(96)	69(1)		9.6(147)	53(1)		9.7(147)	51(1)
			5.0(148)			5.1(424)			5.5(424)	
			3.3(32)			5.0(91)			5.1(91)	
						3.7(161)			4.3(161)	
25	$3s^2\ 3p^3\ 3d\ {}^1G_4$	1.7×10^{-2}	26	74	2.9×10^{-2}	40	60	3.1×10^{-2}	43	57
			5.3(184)	69(1)		6.6(74)	56(1)		7.7(74)	53(1)
			5.1(32)			5.2(32)			5.1(32)	
			4.0(74)			4.4(178)			4.4(178)	
						3.7(423)			4(423)	

Notes. The relative populations POP are given as percentages. RD indicates how much of the population is due to radiative decay from higher levels. EXC indicates how much of the population is due to excitation from lower levels (mostly from the ground state). Following the total percentage, the largest contributions are given, followed by the index in parenthesis of the level from which they originate, using the indexing of Tables 2 and 3. Considerable percentage contributions come from a multitude of levels not displayed here. D10 indicates values calculated with the previous model, while RM4 and RM4+DW6 with the present ion models. In all cases, the values are calculated at log N_e [cm^{-3}] = 8 and log T_e [K] = 6.15.

transitions to the main $n = 4$ levels, calculated with the DW4 target. Table 7 shows the effective collision strengths of the RM4 calculation for a sample of temperatures and transitions to the main $n = 4$ levels.

We then calculated line intensities and looked at how levels are populated at log N_e [cm^{-3}] = 8 and log T_e [K] = 6.15, the electron density of the quiet Sun and the electron temperature of maximum ion abundance in ionisation equilibrium. The brightest lines are listed in Table 8. This table also shows the gf and A values calculated in this work. For comparison, the values calculated by Bhatia et al. (2002) are also shown. Reasonable agreement (20–30%) is found, with the Bhatia et al. (2002) gf values consistently larger than ours. Such differences are to be expected considering the large differences in the targets.

The collision strengths populating a selection of $n = 4$ levels giving rise to some of the strongest soft X-ray transitions are displayed in Figs. 4–9. As expected, excellent agreement between the background R-matrix and the DW collision strengths is found in all cases. Figures 4 and 8 also show the DW collision strengths as calculated by Bhatia et al. (2002), which show good agreement with ours considering the differences in the target.

However, we find significant resonance contribution for transitions to a number of levels, in particular to the $3s^2\ 3p^3\ 4s$ ones, as found for Fe X. One of the strongest lines from these levels

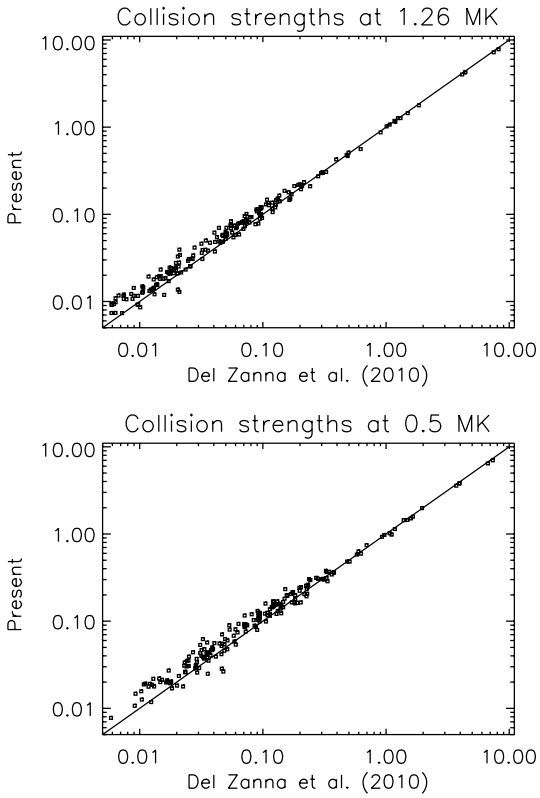

Fig. 2. Thermally-averaged collision strengths for a selection of transitions (see text).

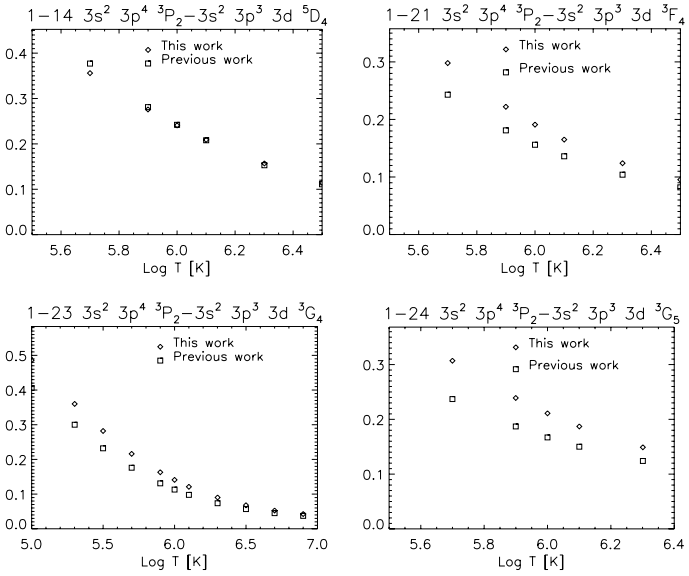

Fig. 3. Thermally-averaged collision strengths for a selection of transitions, important for populating level 14.

is the 1–291 $3s^2\ 3p^4\ {}^3P_2$–$3s^2\ 3p^3\ 4s\ {}^3D_3$ line. Within the RM4 model, the upper level is mainly populated by direct excitation from the ground state (69%), however significant contribution from cascading is present, in particular from the $3s^2\ 3p^3\ 4p\ {}^3P_2$ (level 454, 23%). Figure 4 shows the collision strength for the 1−291 transition, showing a strong enhancement (almost a factor of two), due to resonances.

As we found in the Fe X case, there is a forbidden transition from the ground state to one of the $3s\ 3p^4\ 4s$ levels (596, $^3P_2$) with a collision strength larger than those for the

Table 6. Collision strengths of the DW4 calculation for a sample of transitions to the main $n = 4$ levels.

$i-j$	0.00	0.80	2.24	4.82	9.48	17.80	32.90	60.00
1–265	2.5^{-2}	2.8^{-2}	3.2^{-2}	4.1^{-2}	5.6^{-2}	9.2^{-2}	1.4^{-1}	1.3^{-1}
1–289	1.3^{-2}	1.4^{-2}	1.6^{-2}	1.9^{-2}	2.5^{-2}	3.9^{-2}	5.7^{-2}	5.6^{-2}
1–291	2.6^{-2}	2.9^{-2}	3.3^{-2}	4.0^{-2}	5.5^{-2}	8.6^{-2}	1.3^{-1}	1.3^{-1}
1–377	6.1^{-2}	6.1^{-2}	6.2^{-2}	6.2^{-2}	6.4^{-2}	6.5^{-2}	6.6^{-2}	6.7^{-2}
1–424	3.2^{-2}	3.3^{-2}	3.4^{-2}	3.6^{-2}	4.0^{-2}	4.3^{-2}	4.6^{-2}	5.1^{-2}
1–454	6.4^{-1}	6.5^{-1}	6.7^{-1}	6.9^{-1}	7.1^{-1}	7.3^{-1}	7.5^{-1}	7.6^{-1}
1–460	5.5^{-2}	5.6^{-2}	5.6^{-2}	5.8^{-2}	6.0^{-2}	6.2^{-2}	6.3^{-2}	6.4^{-2}
1–536	2.8^{-2}	3.1^{-2}	3.5^{-2}	4.4^{-2}	6.3^{-2}	1.0^{-1}	1.5^{-1}	1.8^{-1}
1–596	4.9^{-1}	4.9^{-1}	5.0^{-1}	5.2^{-1}	5.5^{-1}	5.7^{-1}	5.9^{-1}	6.1^{-1}
1–749	9.0^{-2}	9.3^{-2}	9.7^{-2}	1.0^{-1}	1.2^{-1}	1.4^{-1}	1.6^{-1}	1.8^{-1}
1–813	1.3^{-1}	1.3^{-1}	1.4^{-1}	1.6^{-1}	1.9^{-1}	2.3^{-1}	2.7^{-1}	3.2^{-1}

Notes. The first column indicates the lower and upper levels of the transition, the rest are the collision strengths at the final energy values (Ryd) indicated in the first row. a^b Indicates $a \times 10^b$.

Table 7. Effective collision strengths of the RM4 calculation for a sample of temperatures and transitions to the main $n = 4$ levels.

$i-j$	5.00	5.50	5.90	6.00	6.10	6.30	6.70	8.00
1–265	2.0^{-1}	1.3^{-1}	9.2^{-2}	8.8^{-2}	8.5^{-2}	8.7^{-2}	1.2^{-1}	4.1^{-1}
1–289	1.3^{-1}	7.7^{-2}	4.9^{-2}	4.5^{-2}	4.3^{-2}	4.1^{-2}	5.0^{-2}	1.7^{-1}
1–291	2.4^{-1}	1.5^{-1}	1.0^{-1}	9.3^{-2}	8.9^{-2}	8.8^{-2}	1.1^{-1}	3.8^{-1}
1–377	1.4^{-1}	1.0^{-1}	8.0^{-2}	7.6^{-2}	7.3^{-2}	7.0^{-2}	6.8^{-2}	7.6^{-2}
1–424	8.2^{-2}	5.7^{-2}	4.4^{-2}	4.3^{-2}	4.2^{-2}	4.2^{-2}	4.7^{-2}	7.2^{-2}
1–454	6.7^{-1}	6.6^{-1}	6.6^{-1}	6.7^{-1}	6.7^{-1}	6.9^{-1}	7.1^{-1}	7.6^{-1}
1–460	7.0^{-2}	6.3^{-2}	5.9^{-2}	5.9^{-2}	5.9^{-2}	5.9^{-2}	6.1^{-2}	6.6^{-2}
1–536	8.4^{-2}	6.7^{-2}	6.4^{-2}	6.7^{-2}	7.0^{-2}	8.2^{-2}	1.3^{-1}	5.6^{-1}
1–596	4.8^{-1}	4.9^{-1}	5.0^{-1}	5.1^{-1}	5.1^{-1}	5.3^{-1}	5.6^{-1}	6.1^{-1}
1–749	9.0^{-2}	9.3^{-2}	1.0^{-1}	1.0^{-1}	1.1^{-1}	1.2^{-1}	1.5^{-1}	2.3^{-1}
1–813	1.3^{-1}	1.4^{-1}	1.6^{-1}	1.6^{-1}	1.7^{-1}	1.9^{-1}	2.4^{-1}	3.8^{-1}

Notes. The full dataset is available electronically at the CDS. The first column indicates the lower and upper levels of the transition, the rest are the effective collision strengths at the log T_e[K] values indicated in the first row. a^b Indicates $a \times 10^b$.

$-3s^2\ 3p^3\ 4s$ lines, as shown in Fig. 5. This transition is not affected by resonances or cascading from higher levels. The decays from this level produce some spectral lines (unidentified) that are predicted to be very strong at coronal densities. In particular, the $3s\ 3p^5\ {}^3P_2$–$3s\ 3p^4\ 4s\ {}^3P_2$ is the strongest Fe XI soft X-ray line. They were not identified by B.C. Fawcett because of their small gf values.

Some of the main $3s^2\ 3p^3\ 4p$ levels are affected by resonance enhancements and cascading. Figure 6 shows as an example the collision strength for the 1–424 transition. Level 424 ($^3F_4$) is populated by cascading and by direct excitation from the ground state (76% with the RM4 model). Level 454 ($3s^2\ 3p^3\ 4p\ {}^3P_2$) on the other hand is populated via direct excitation from the ground state, with a large collision strength, shown in Fig. 7. Its main radiative decay is to level 6, via a strong unidentified transition. This transition also has a small gf value, hence was not identified by B.C. Fawcett.

The other $n = 4$ levels are generally less affected by resonance enhancements and radiative decays, at least with the present RM4 model. Figure 8 shows the main collision strength populating $3s^2\ 3p^3\ 4d\ {}^3D_3$, producing the strongest decay from this configuration (to the ground state). Figure 9 shows the main collision strength populating the $3s^2\ 3p^3\ 4f\ {}^3F_4$ level, which in

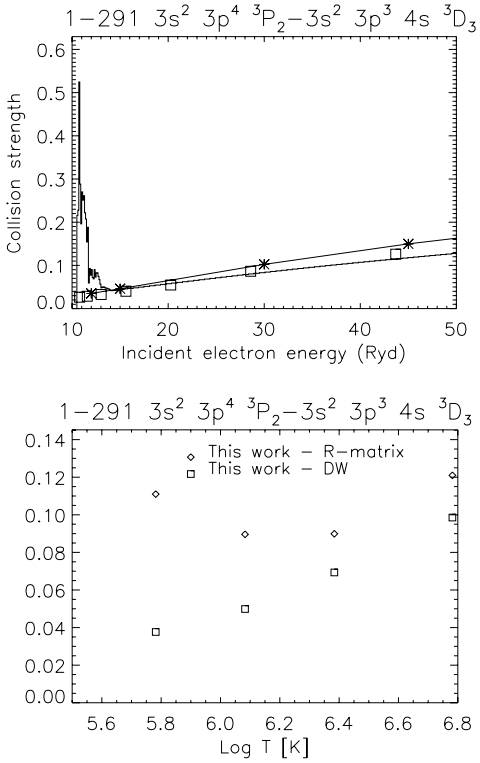

Fig. 4. *Upper panel*: collision strength for the 1–291 transition, averaged over 0.1 Ryd in the resonance region. The data points are displayed in histogram mode. Boxes indicate our DW values, while asterisks the DW values of Bhatia et al. (2002). *Lower panel*: thermally-averaged collision strengths.

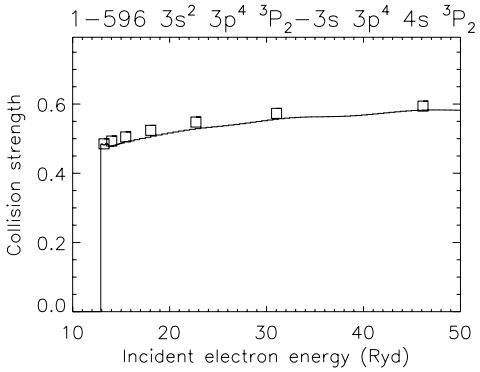

Fig. 5. Collision strength for the 1–596 transition.

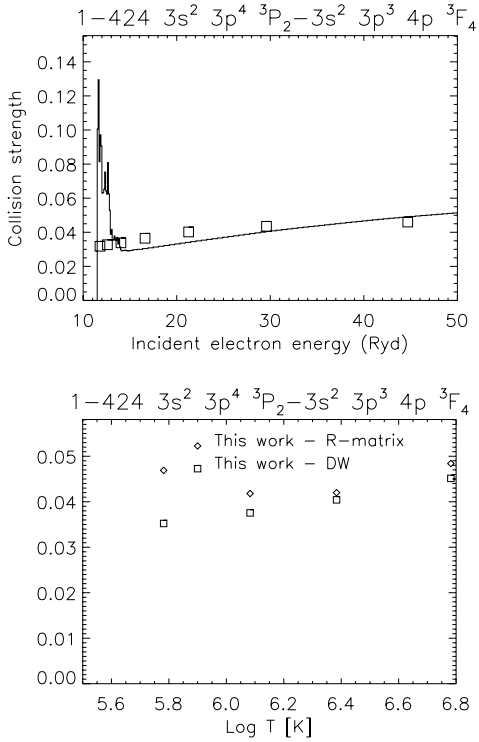

Fig. 6. Same as Fig. 4, for the 1–424 transition.

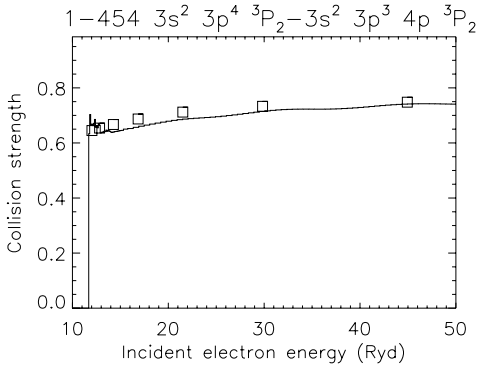

Fig. 7. Collision strength for the 1–454 transition.

turn has its main decay to the $3s^2\ 3p^3\ 3d\ ^3D_3$. This is one of the many 4f → 3d transitions that are present near the important 94 Å Fe X line (Del Zanna et al. 2012b), where the SDO AIA 94 Å band has its peak sensitivity. Some of the lines in this transition array were only tentatively identified by B.C. Fawcett.

4.4. DW calculations for the n = 5, 6 levels

To estimate the effects of further cascading from even higher levels, we built a new target by adding a selection of main $n = 5, 6$ configurations to the R-matrix $n = 4$ one (RM4), listed in Table 1. We kept the scaling parameters for the $n = 4$ orbitals the same, and obtained those for the $n = 5, 6$, which are also listed in Table 1. This was done to try and keep similar energies (and ordering of the levels) for the $n = 4$ levels. The total target comprises 66 configurations and 6085 levels, however only 50 configurations were retained for the DW calculation. The following were kept as correlation: $3s^2\ 3p^2\ 3d\ 4l$ (l = p, d, f), $3s\ 3p^3\ 3d\ 4l$ (l = s, p, d, f), $3p^5\ 4l$ (l = s, p, d, f),$3p^4\ 3d\ 4l$ (l = s, p, d, f), and $3p^3\ 3d^3$. This model produces 2478 levels. We then used the DW code to calculate the excitation rates up to all of these levels, but just from the 47 levels arising from the $3s^2\ 3p^4$, $3s\ 3p^5$, and $3s^2\ 3p^3\ 3d$ configurations. This number was chosen to include all metastable levels which may contribute to the populations of the remaining levels.

We then calculated separately the radiative rates between all the 2478 levels, matched the ordering of these levels with that of the 996-levels RM4 and then merged the excitation rates and A-values from RM4 with those from this DW run. The resulting ion population model we call RM4 + DW6.

The relative intensities of the main soft X-ray lines as obtained with the RM4 + DW6 model are also shown in Table 8. Cascading from the $n = 5, 6$ levels generally increases the intensities of the $n = 4 \rightarrow n = 3$ transitions by small amounts, of

Table 8. Relative intensities of the brightest Fe XI lines in the soft X-rays.

$i-j$	Levels	*Int* 1.0×10^{8} DW4	*Int* 1.0×10^{8} RM4	*Int* 1.0×10^{8} RM4+DW6	*Int* 1.0×10^{12} RM4	gf	$A_{ji}(s^{-1})$	λ_{exp}(Å)	λ_{th}(Å)
6–596	$3s\ 3p^5\ ^3P_2$–$3s\ 3p^4\ 4s\ ^3P_2$	1.8×10^{-2}	1.8×10^{-2}	1.8×10^{-2}	7.9×10^{-3}	0.46	7.7×10^{10}	88.933*	85.51 (−3.4)
6–454	$3s\ 3p^5\ ^3P_2$–$3s^2\ 3p^3\ 4p\ ^3P_2$	1.3×10^{-2}	1.4×10^{-2}	1.4×10^{-2}	6.0×10^{-3}	8.3×10^{-2}	1.1×10^{10}	100.575*	96.36 (−4.2)
1–291	$3s^2\ 3p^4\ ^3P_2$–$3s^2\ 3p^3\ 4s\ ^3D_3$	6.0×10^{-3}	8.7×10^{-3}	9.7×10^{-3}	5.2×10^{-3}	0.37(0.51)	$4.5(6.6)\times10^{10}$	86.772	84.52 (−2.3)
1–265	$3s^2\ 3p^4\ ^3P_2$–$3s^2\ 3p^3\ 4s\ ^3S_1$	3.7×10^{-3}	5.3×10^{-3}	5.8×10^{-3}	3.2×10^{-3}	0.39(0.50)	$1.1(1.4)\times10^{11}$	89.185	86.85 (−2.3)
42–454	$3s^2\ 3p^3\ 3d\ ^3D_3$–$3s^2\ 3p^3\ 4p\ ^3P_2$	5.1×10^{-3}	5.1×10^{-3}	5.2×10^{-3}	2.3×10^{-3}	5.8×10^{-2}	4.1×10^{9}	138.21*	132.77 (−5.4)
7–596	$3s\ 3p^5\ ^3P_1$–$3s\ 3p^4\ 4s\ ^3P_2$	4.4×10^{-3}	4.5×10^{-3}	4.5×10^{-3}	1.9×10^{-3}	0.12	1.9×10^{10}	89.703*	86.20 (−3.5)
7–454	$3s\ 3p^5\ ^3P_1$–$3s^2\ 3p^3\ 4p\ ^3P_2$	4.1×10^{-3}	4.2×10^{-3}	4.2×10^{-3}	1.8×10^{-3}	2.6×10^{-2}	3.3×10^{9}	101.559*	97.25 (−4.3)
1–536	$3s^2\ 3p^4\ ^3P_2$–$3s^2\ 3p^3\ 4d\ ^3D_3$	3.1×10^{-3}	3.9×10^{-3}	5.0×10^{-3}	2.0×10^{-3}	0.73(0.98)	$1.3(1.8)\times10^{11}$	72.635	70.98 (−1.7)
38–454	$3s^2\ 3p^3\ 3d\ ^3P_2$–$3s^2\ 3p^3\ 4p\ ^3P_2$	3.8×10^{-3}	3.9×10^{-3}	3.9×10^{-3}	1.7×10^{-3}	4.1×10^{-2}	3.0×10^{9}	133.95*	128.40 (−5.5)
16–749	$3s^2\ 3p^3\ 3d\ ^3D_3$–$3s^2\ 3p^3\ 4f\ ^3F_4$	3.7×10^{-3}	3.8×10^{-3}	3.9×10^{-3}	1.9×10^{-3}	3.40	2.9×10^{11}	–	89.77
42–813	$3s^2\ 3p^3\ 3d\ ^3D_3$–$3s^2\ 3p^3\ 4f\ ^3F_4$	3.1×10^{-3}	3.2×10^{-3}	3.2×10^{-3}	1.6×10^{-3}	2.31	1.6×10^{11}	–	99.64
16–377	$3s^2\ 3p^3\ 3d\ ^3D_3$–$3s^2\ 3p^3\ 4p\ ^3P_2$	2.3×10^{-3}	2.7×10^{-3}	2.9×10^{-3}	1.5×10^{-3}	0.16	1.3×10^{10}	–	119.93
24–424	$3s^2\ 3p^3\ 3d\ ^3G_5$–$3s^2\ 3p^3\ 4p\ ^3F_4$	2.1×10^{-3}	2.5×10^{-3}	2.8×10^{-3}	2.2×10^{-3}	0.47	2.2×10^{10}	123.490	120.03 (−3.5)
2–265	$3s^2\ 3p^4\ ^3P_1$–$3s^2\ 3p^3\ 4s\ ^3S_1$	1.7×10^{-3}	2.4×10^{-3}	2.6×10^{-3}	1.5×10^{-3}	0.18(0.23)	$4.8(6.3)\times10^{10}$	90.204	87.79 (−2.4)
1–289	$3s^2\ 3p^4\ ^3P_2$–$3s^2\ 3p^3\ 4s\ ^3D_2$	1.4×10^{-3}	2.3×10^{-3}	2.5×10^{-3}	1.9×10^{-3}	0.16(0.21)	$2.8(3.8)\times10^{10}$	87.025	84.71 (−2.3)
39–454	$3s^2\ 3p^3\ 3d\ ^3S_1$–$3s^2\ 3p^3\ 4p\ ^3P_2$	2.2×10^{-3}	2.3×10^{-3}	2.3×10^{-3}	9.9×10^{-4}	2.4×10^{-2}	1.8×10^{9}	134.34*	129.08 (−5.2)
30–460	$3s^2\ 3p^3\ 3d\ ^3F_3$–$3s^2\ 3p^3\ 4p\ ^3D_2$	2.0×10^{-3}	2.1×10^{-3}	2.2×10^{-3}	1.5×10^{-3}	0.20	1.7×10^{10}	123.572	120.21 (−3.4)
1–42	$3s^2\ 3p^4\ ^3P_2$–$3s^2\ 3p^3\ 3d\ ^3D_3$	1.0	1	1	0.44	4.82	1.5×10^{11}	180.401	176.36 (−4.0)

Notes. The lines are displayed in decreasing order of intensity (photons) $Int = N_j A_{ji}/N_e$ relative to the strongest EUV line. The intensities were calculated at log T_e [K] = 6.15. Columns 3, 4, 5 show the relative intensities calculated at log N_e [cm^{-3}] = 8 with the DW4, RM4, and RM4+DW6 ion models. Column 6 shows the values at log N_e [cm^{-3}] = 12 from the RM4 ion model. Columns 7, 8 show the gf and A values calculated in this work. The values in brackets are those calculated by Bhatia et al. (2002). The next column shows the experimental wavelengths. Values indicated with * are from Del Zanna (2012), the others are from Fawcett et al. (1972). The last column shows the wavelengths corresponding to the target energies. Values in parenthesis give the corresponding wavelength difference with the experimental ones.

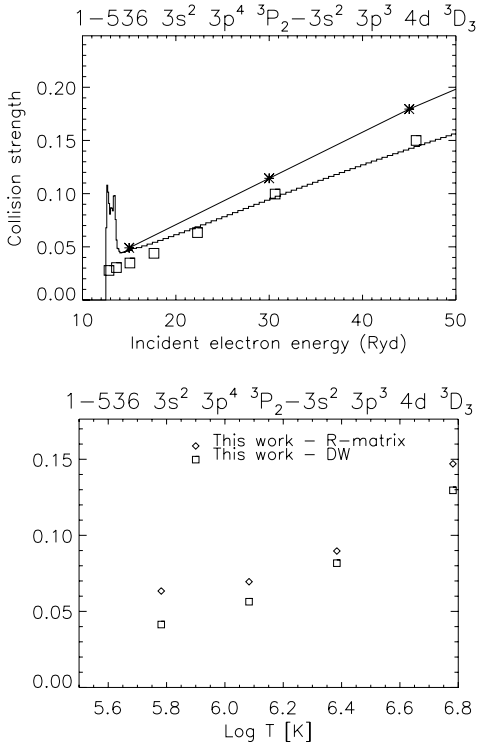

Fig. 8. Same as Fig. 4, for the 1–536 transition.

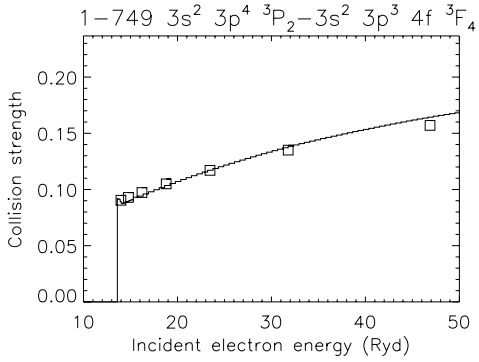

Fig. 9. Collision strength for the 1–749 transition.

the order of 10–20% at most for the strongest transitions listed in the Table.

5. Conclusions

We have presented the first large-scale R-matrix calculations for the $n = 4$ levels in Fe XI. We have found the same issues we discovered in Fe X (Del Zanna et al. 2012b) and found to be present in Fe XII (Del Zanna et al. 2012a) and Fe XIII (Del Zanna & Storey 2012), i.e. resonance enhancement for some $n = 4$ configurations and levels is significant. We conclude that cascading is generally not a major effect but we have listed a few levels which are exceptions. Cascading from the $n = 5, 6$ level is a minor effect.

As in the Fe X case, we found a large number of strong lines at coronal densities which are unidentified. Indeed most of the lines which are predicted to be strongest are unidentified. The identifications of some of these lines will be discussed in a separate paper.

As in the Fe XII case, we found a subtle effect, i.e. a number of lower $n = 3$ levels with enhanced populations, caused by increased cascading from higher $n = 3$ levels whose collision strengths are enhanced compared to our previous work.

Acknowledgements. G.D.Z. acknowledges the support from STFC via the Advanced Fellowship programme. We acknowledge support from STFC for the UK APAP network.

References

Badnell, N. R. 1997, J. Phys. B At. Mol. Phys., 30, 1
Badnell, N. R. 2011, Comput. Phys. Commun., 182, 1528
Badnell, N. R., & Griffin, D. C. 2001, J. Phys. B At. Mol. Phys., 34, 681
Behring, W. E., Cohen, L., Doschek, G. A., & Feldman, U. 1976, ApJ, 203, 521
Berrington, K. A., Eissner, W. B., & Norrington, P. H. 1995, Comput. Phys. Commun., 92, 290
Bhatia, A. K., Doschek, G. A., & Eissner, W. 2002, At. Data Nucl. Data Tables, 82, 211
Brinkman, A. C., Gunsing, C. J. T., Kaastra, J. S., et al. 2000, ApJ, 530, L111
Burgess, A. 1974, J. Phys. B At. Mol. Phys., 7, L364
Burgess, A., Chidichimo, M. C., & Tully, J. A. 1997, J. Phys. B At. Mol. Phys., 30, 33
Burgess, A., & Tully, J. A. 1992, A&A, 254, 436
Chidichimo, M. C., Badnell, N. R., & Tully, J. A. 2003, A&A, 401, 1177
Del Zanna, G. 2010, A&A, 514, A41
Del Zanna, G. 2012, A&A, 546, A97
Del Zanna, G., & Storey, P. J. 2012, A&A, 543, A144
Del Zanna, G., Storey, P. J., & Mason, H. E. 2010, A&A, 514, A40
Del Zanna, G., Storey, P. J., Badnell, N. R., & Mason, H. E. 2012a, A&A, 543, A139
Del Zanna, G., Storey, P. J., Badnell, N. R., & Mason, H. E. 2012b, A&A, 541, A90
Edlén, B. 1937, Z. Astrophys., 104, 407
Fawcett, B. C., Peacock, N. J., & Cowan, R. D. 1968, J. Phys. B At. Mol. Phys., 1, 295
Fawcett, B. C., Kononov, E. Y., Hayes, R. W., & Cowan, R. D. 1972, J. Phys. B At. Mol. Phys., 5, 1255
Griffin, D. C., Badnell, N. R., & Pindzola, M. S. 1998, J. Phys. B At. Mol. Phys., 31, 3713
Hummer, D. G., Berrington, K. A., Eissner, W., et al. 1993, A&A, 279, 298
Landi, E., Young, P. R., Dere, K. P., Del Zanna, G., & Mason, H. E. 2012, ApJ, submitted
Lemen, J. R., Title, A. M., Akin, D. J., et al. 2012, Sol. Phys., 275, 17
Manson, J. E. 1972, Sol. Phys., 27, 107
O'Dwyer, B., Del Zanna, G., Badnell, N. R., Mason, H. E., & Storey, P. J. 2012, A&A, 537, A22
Woods, T. N., Eparvier, F. G., Hock, R., et al. 2012, Sol. Phys., 275, 115